Inventory of Supplementary Materials

Figure S1 (related to Figure 2). MRCK-1 depletion blocks both posterior and anterior contraction phases during maintenance.

Figure S2 (related to Figure 3). Loss of PAR-6 asymmetry in chin-1(tm1909);par-1(RNAi) is independent of cortical flow.

Figure S3 (related to Figure 4). Further analysis of PAR-3::GFP cluster distributions in wild type and mutant embryos. Comparison of par-3(crispr)::PAR-3::GFP and par-3(tg)::PAR-3::GFP.

Figure S4 (related to Figure 5). Regulation of spatial but not temporal distributions of CHIN-1 cluster growth by other polarity proteins.

Figure S5 (related to Figure 7). Using empirical observations to constrain key model parameters.

Figure S6 (related to Figure 7). Analysis of CHIN-1 and PAR-3 mobilities during maintenance phase.

Movie S1 (related to Figure 2). Dynamics of GFP::PAR-6 in control, *par-2(lw32)*, and *par-2(lw32);lgl-1(tm2616)* mutant embryos.

Movie S2 (related to Figure 2). Dynamics of GFP::PAR-6 in control, *par-2(lw32)*, and *par-2(lw32);lgl-1(tm2616)* mutant embryos that were subjected to *mrck-1(RNAi)*.

Movie S3 (related to Figure 3). Dynamics of GFP::PAR-6 in control and *par-1(RNAi*) embryos.

Movie S4 (related to Figure 3). Dynamics of GFP::PAR-6 in *chin-1(tm1909)* mutants embryos combined with *mrck-1(RNAi)*, *par-1(RNAi)*, and *par-1(RNAi);mrck-1(RNAi)*.

Movie S5 (related to Figure 4). Dynamics of PAR-3::GFP in wild type and *par-1(RNAi)* embryos.

Movie S6 (related to Figure 4). Single molecules of GFP::PAR-6 in control, *chin-1(tm1909);mrck-1(RNAi)*, *par-1(RNAi)*, and *chin-1(tm1909);par-1(RNAi)* embryos.

Movie S7 (related to Figures 5 and 6). Dynamics of CHIN-1::GFP in a wild type embryo.

Supplementary Experimental Procedures

Supplementary Modeling Procedures

Supplementary References

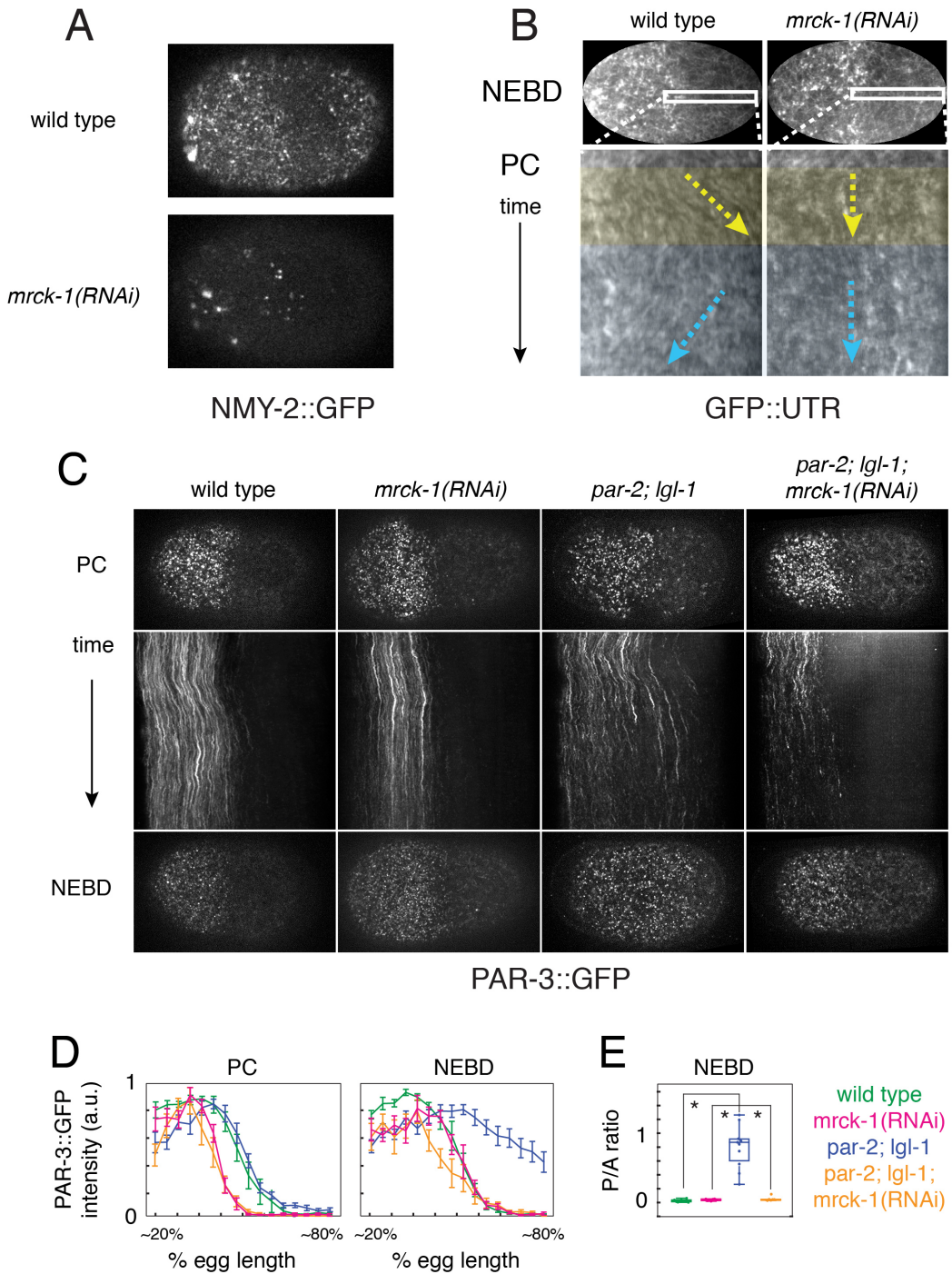

Figure S1 (related to Figure 2). MRCK-1 depletion blocks both posterior and anterior contraction phases during maintenance. (A) Comparison of wild-type and *mrck-1(RNAi)* embryos expressing NMY-2::GFP just after maintenance phase onset when posterior contraction

normally occurs. Note that NMY-2::GFP is completely absent from the posterior pole. (B) Still images and kymographs from wild-type and *mrck-1(RNAi)* embryos expressing the F-actin binding domain of Utrophin fused to GFP (GFP::UTR). White rectangles over still images indicate the regions used to construct the kymographs. Yellow and blue shading indicates posterior and anterior contraction phases corresponding to those shown in Figure 2A,C,D. Arrows indicate the direction and speed of cortical flows. (C) Cortical movements of PAR-3::GFP in wild-type, *mrck-1(RNAi)*, *par-2(lw32);lgl-1(tm2616)*, and *par-2(lw32);lgl-1(tm2616);mrck-1(RNAi)* embryos. Top row shows surface views of cortical PAR-3::GFP at late pseudocleavage (PC); bottom row shows the same embryos at nuclear envelope breakdown (NEBD). Kymographs show dynamics of PAR-3::GFP distribution between PC and cleavage. (D) Fluorescence intensity profiles of PAR-3::GFP at maintenance onset (left) and NEBD (right). Profiles correspond to wild-type (green; n = 10), *mrck-1(RNAi)* (magenta; n = 7), *par-2(lw32);lgl-1(tm2616)* (orange; n = 11), and *par-2(lw32);lgl-1(tm2616);mrck-1(RNAi)* (blue; n = 6) embryos. Error bars indicate +/- 1 SEM. (E) Box and whisker plots showing the distributions of Posterior::Anterior intensity ratios for the data in (D). Colored circles indicate individual data points. * indicates $p < 0.0001$ by Students T test.

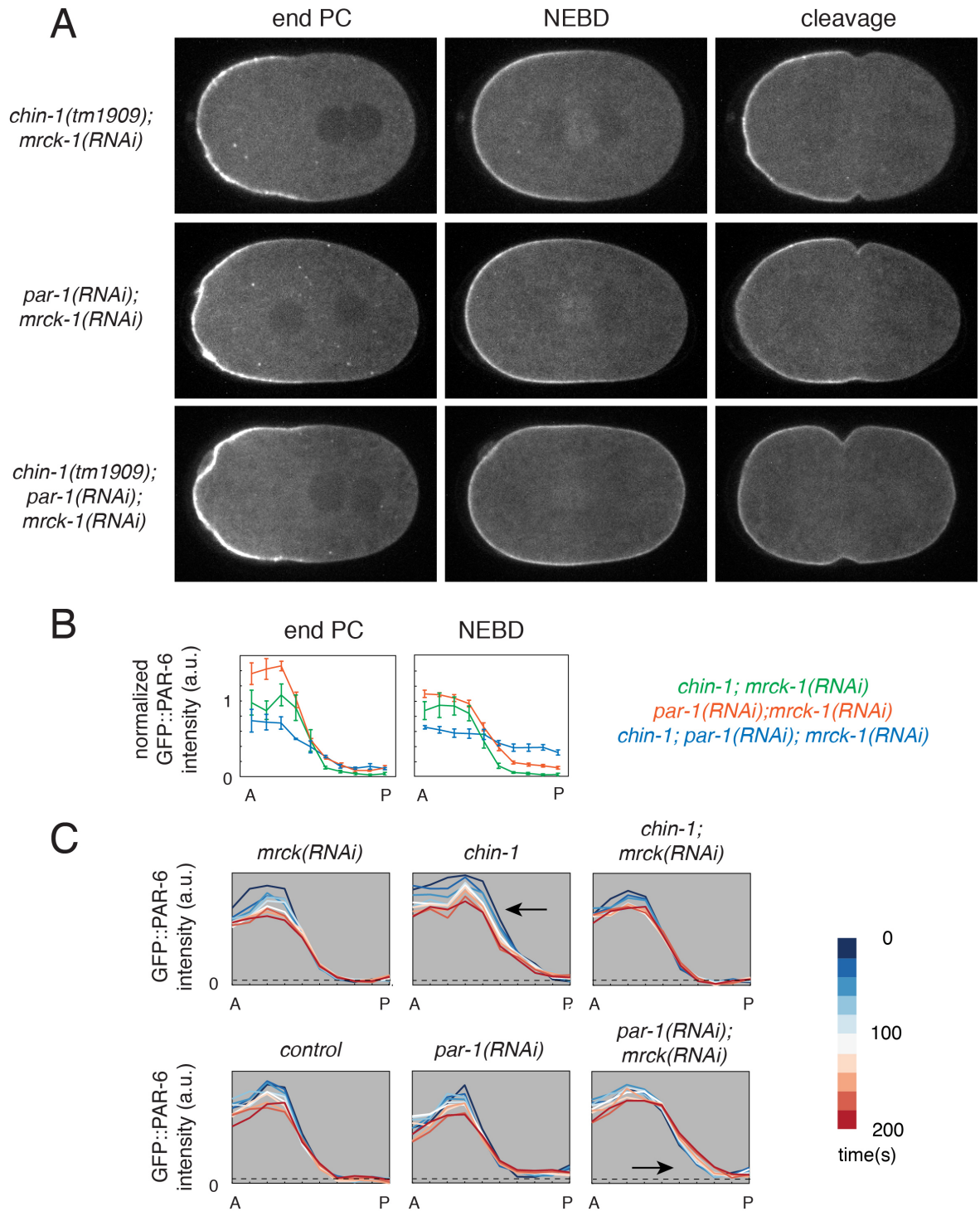

Figure S2 (related to Figure 3). Loss of PAR-6 asymmetry in *chin-1(tm1909);par-1(RNAi)* is independent of cortical flow. (A) Equatorial views of GFP::PAR-6 at the end of Pseudocleavage (end PC), nuclear envelope breakdown (NEBD), and cleavage in

chin-1(tm1909);mrck-1(RNAi) and *chin-1(tm1909);par-1(RNAi);mrck-1(RNAi)* embryos. (B) Normalized fluorescence intensity profiles of GFP::PAR-6 at end PC (top) and NEBD (bottom) in *chin-1(tm1909); mrck-1(RNAi)* (solid lines) and *chin-1(tm1909);par-1(RNAi);mrck-1(RNAi)* (dashed lines) embryos. Values of 0 and 1 correspond to extreme anterior and posterior, respectively. Error bars indicate +/- 1 SEM. (C) Kymographs showing redistribution of GFP::PAR-6 during maintenance phase in *chin-1(tm1909);par-1(RNAi)* and *chin-1(tm1909); par-1(RNAi);mrck-1(RNAi)* embryos. Yellow and blue shading indicates posterior and anterior contraction phases corresponding to those shown in Figure 2A,B,D,E. Yellow and blue arrows indicate the approximate directions of cortical flow near the edge of the anterior PAR domain. (D) GFP::PAR-6 intensity profiles measured for the indicated conditions at 20 sec intervals during maintenance phase in single embryos. Heatmap indicates time relative to NEBD. Solid arrows indicate the direction of boundary drift.

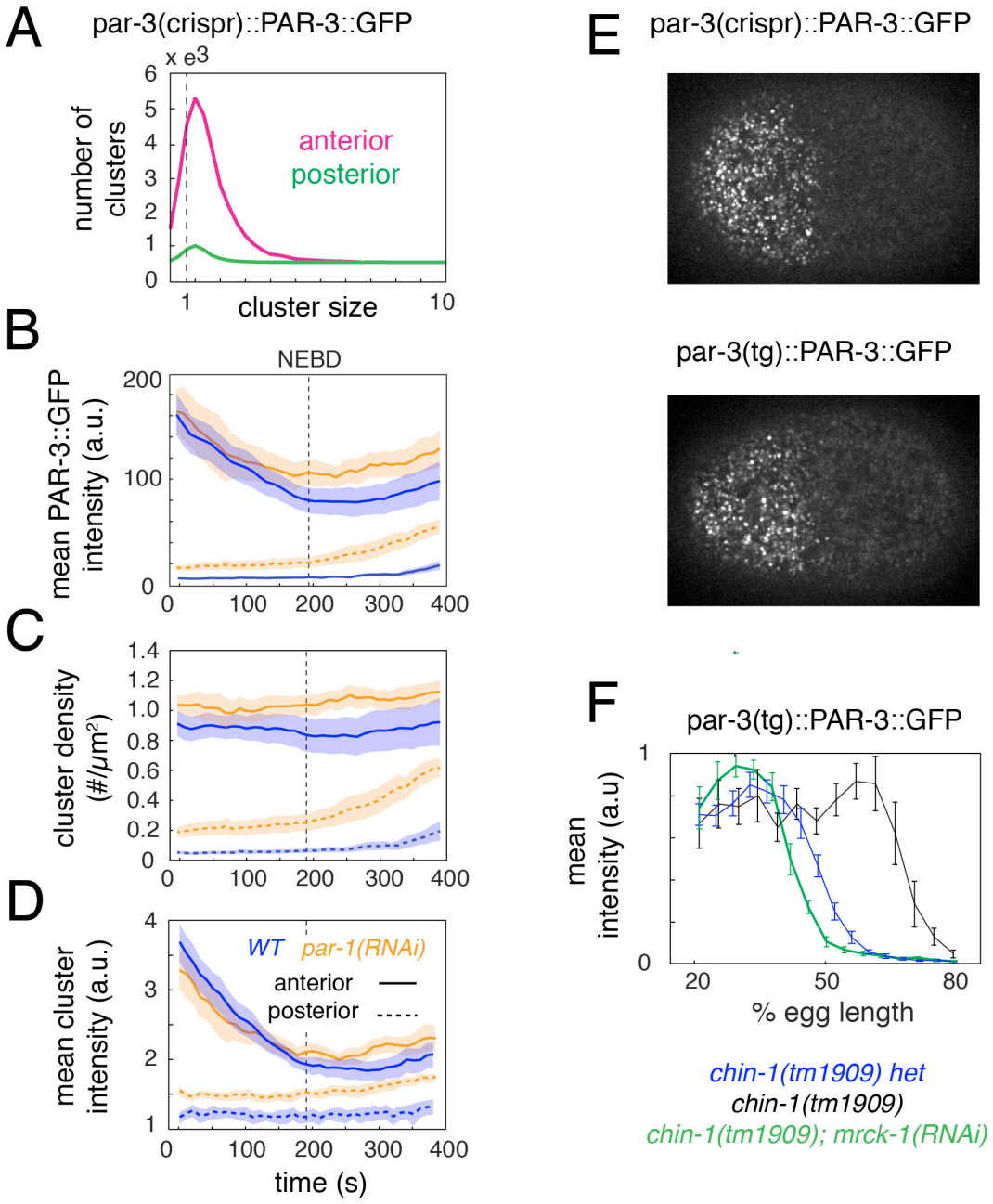

Figure S3 (related to Figure 4). Further analysis of PAR-3::GFP cluster distributions. (A) Distribution of anterior (magenta) and posterior (green) PAR-3::GFP cluster sizes in early maintenance. Vertical dashed line indicates the mean intensity of single molecules of PAR-3::GFP measured under the same conditions (see Supplementary Experimental Procedures). (B-D) Plots of mean PAR-3::GFP intensity (B), cluster density (C) and mean cluster intensity (D)

vs. time within anterior (solid line) and posterior (dashed line) domains, in either wild-type (blue lines) or *par-1(RNAi)* (orange lines) embryos. Data were aligned in time with respect to onset of maintenance phase (t = 0s). Halos indicate +/- 1 SEM (n = 5 embryos). (D) Comparison of PAR-3::GFP distribution at early maintenance in strains expressing PAR-3::GFP as a knock-in at the endogenous locus (top) or as a transgene at a separate locus (bottom). (E) PAR-3::GFP intensity vs. AP position at NEBD in wild-type (blue; n = 6), *chin-1(tm1909)* (black; n = 5), and *chin-1(tm1909);mrck-1(RNAi) (green; n = 6)* embryos. Data for wild type and *chin-1(tm1909);mrck-1(RNAi)* are the same as in Figure 4E. For each curve, error bars indicate +/- 1 SEM .

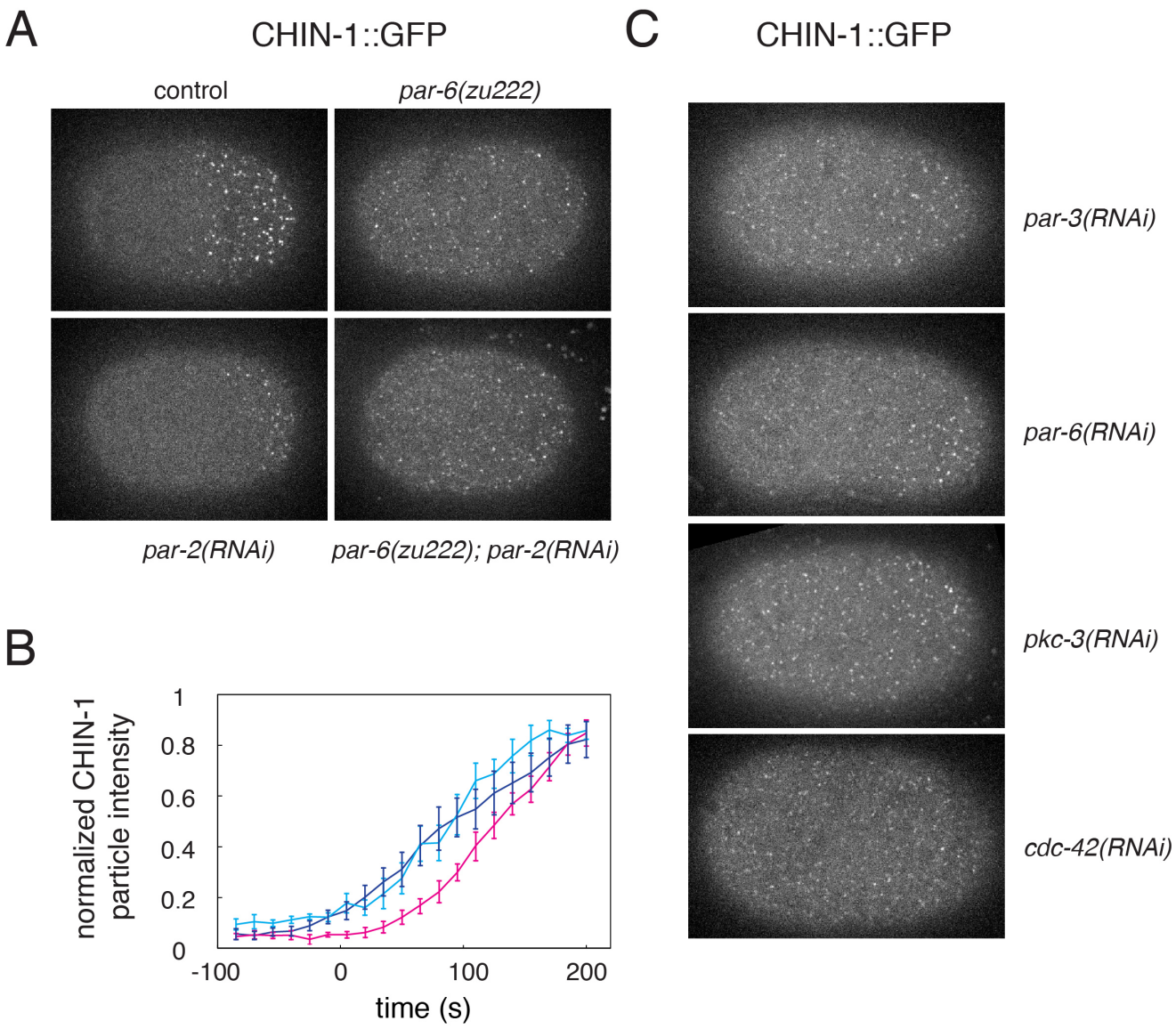

Figure S4 (related to Figure 5). Regulation of spatial but not temporal distributions of CHIN-1 cluster growth by other polarity proteins. (A) Distributions of CHIN-1::GFP clusters at late maintenance phase in embryos of the indicated genotypes and RNAi conditions. Embryos used for control and *par-2(RNAi)* are *par-6(zu222)* heterozygotes. (B) Plots of CHIN-1::GFP intensity (cluster density * mean cluster intensity) vs time in control (blue), *par-6(zu222)*

(magenta), and *par-2(RNAi)* (cyan) embryos. Error bars indicate +/- 1 SEM (n = 5 embryos for each condition). Data for individual embryos were scaled by the maximum value over all time points and aligned relative to the onset of maintenance (t = 0s). For control and *par-2(RNAi)* embryos, we determined maintenance phase onset as the onset of pseudocleavage furrow relaxation as in other experiments. For *par-6(zu222)* homozygotes, the pseudocleavage furrow is often not well defined, and therefore we determined maintenance phase onset as the onset of the posterior contraction phase. (C) CHIN-1::GFP clusters are also uniformly distributed in *par-3(RNAi)*, *par-6(RNAi)*, *pkc-3(RNAi),* and *cdc-42(RNAi)* embryos.

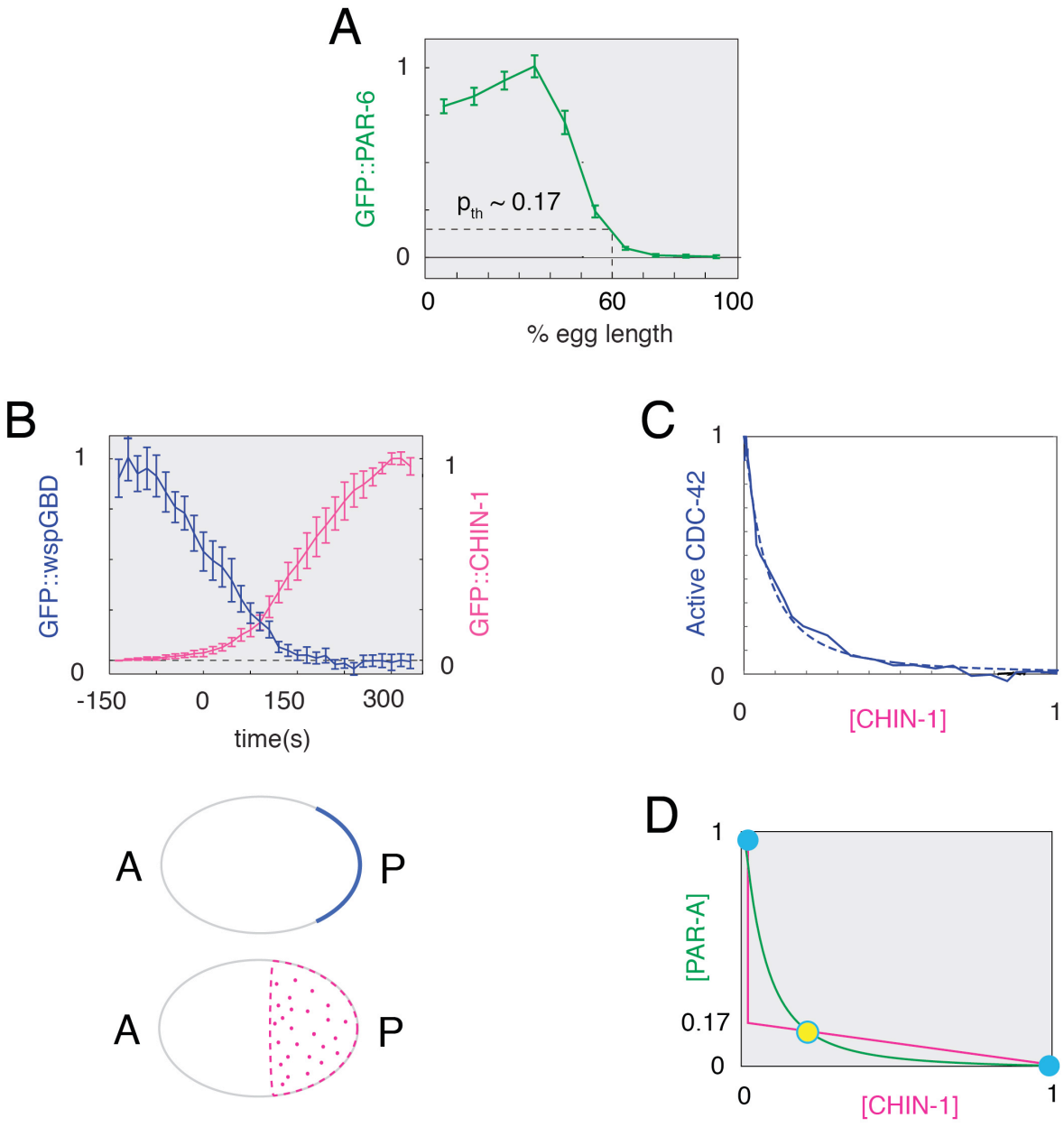

Figure S5 (related to Figure 7). Using empirical observations to constrain key model parameters. (A) Comparing the axial position (~60% egg length; Figure 7I) at which CHIN-1 clusters switch from growth to decay to the steady state distribution of GFP::PAR-6 identifies the threshold level of PAR-6 (as a fraction of its maximum value) at which the switch occurs. (B) Fluorescence intensities for GFP::wspGBD (blue; n = 12) and CHIN-1::GFP (magenta; n = 8) measured in the posterior domain and plotted as a function of time. Curves for individual

embryos are aligned to the onset of maintenance (t = 0s). Schematic diagrams below the graphs indicate the domains in which the measurements were made. The blue curve is identical to that shown in Figure 2B. Error bars indicate +/- 1 SEM. (C) A plot of CHIN-1 vs active CDC-42 constructed by plotting the mean values for the two probes shown in (B) at corresponding time points against one another. Dashed line indicates the approximation:

$$[CDC42] = \frac{1}{1 + 13.3 * [CHIN1] + 61.8 * [CHIN1]^2}$$

that was used in the numerical solutions of the full reaction diffusion system. (D) Projection of steady state solutions of the model equations (see Supplementary Experimental Procedures, Modeling procedures) into the CHIN-1/PAR-A phase plane, where PAR-A refers to the CDC-42/ PAR-6/PKC-3 trimer. Green curve shows steady state dependence of [PAR-A] on CHIN-1 cluster density taken from the analysis in (B) and (C); magenta curve shows steady state dependence of CHIN-1 cluster density on [PAR-A], using the threshold value from (A). Steady states occur where the two curves cross. Solid blue circles indicate stable steady states; Yellow circle with blue border indicates an unstable steady state.

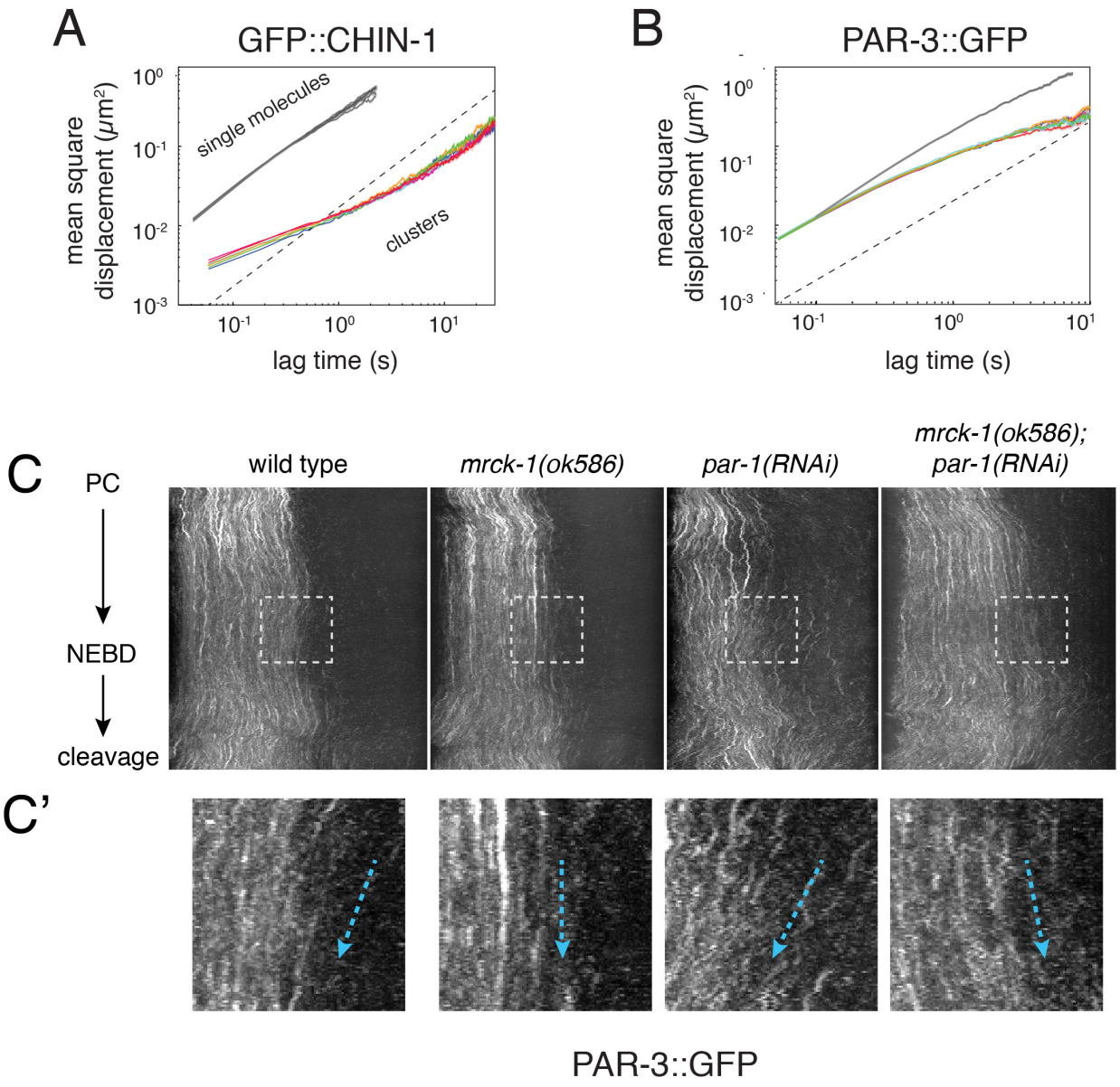

Figure S6 (related to Figure 7). Analysis of CHIN-1 and PAR-3 mobilities.

(A) Mean square square displacement (MSD) vs time measured for CHIN-1 clusters in *mrck-1* mutant embryos to avoid the confounding effects of cortical flow. Colored curves represent independent measurements for 6 different wild type embryos. Grey curves represent measurements of single molecule mobilities for 6 embryos that were treated with *gfp(RNAi)* to reduce expression of the CHIN-1::GFP transgene. For each curve, the solid line and halo indicate

mean +/- 1 SEM. Dashed line indicates the slope of 1 predicted for pure brownian diffusion. (B) MSD vs time measured for PAR-3 clusters during maintenance phase. Colored curves represent independent measurements for 6 different wild type embryos. Grey curves represent independent measurements for 6 embryos that were permeabilized and treated with 10µm Latrunculin A just before onset of maintenance phase. For each curve, the solid line and halo indicate mean +/- 1 SEM. Dashed line indicates the slope of 1 predicted for pure brownian diffusion. (C) Kymographs showing cortical movements of PAR-3::GFP between PC and cleavage in wild-type, *mrck-1(RNAi), par-1(RNAi)*, and *mrck-1(RNAi);par-1(RNAi)* embryos. (C') magnification of regions indicated by dashed lines in C showing cortical movements of PAR-3 clusters near the edge of the anterior domain during the anterior contraction phase. Arrows indicate general direction and speed of cortical flow.

Supplementary Movie Legends

Movie S1 (related to Figure 2). Dynamics of GFP::PAR-6 in control, *par-2(lw32)*, and *par-2(lw32);lgl-1(tm2616)* mutant embryos. Movies run from late pseudocleavage to late maintenance phase. Time compression = 150:1.

Movie S2 (related to Figure 2). Dynamics of GFP::PAR-6 in control, *par-2(lw32)*, and *par-2(lw32);lgl-1(tm2616)* mutant embryos that were also subjected to *mrck-1(RNAi)*. Movie runs from late pseudocleavage to late maintenance phase. Time compression = 150:1.

Movie S3 (related to Figure 3). Dynamics of GFP::PAR-6 in control and *par-1(RNAi*) embryos. Time compression = 300:1.

Movie S4 (related to Figure 3). Dynamics of GFP::PAR-6 in *chin-1(tm1909)*, *chin-1(tm1909);mrck-1(RNAi)*, *chin-1(tm1909);par-1(RNAi)*, and *chin-1(tm1909);par-1(RNAi);mrck-1(RNAi)* embryos. Movie runs from late pseudocleavage to cleavage. Time compression = 300:1.

Movie S5 (related to Figure 4). Dynamics of PAR-3::GFP in wild type and *par-1(RNAi)* embryos. Time compression = 60:1.

Movie S6 (related to Figure 4). Single molecules of GFP::PAR-6 in control, *chin-1(tm1909);mrck-1(RNAi)*, *par-1(RNAi)*, and *chin-1(tm1909);par-1(RNAi)* embryos. All movies were taken during early maintenance phase. Time compression = 1.5:1.

Movie S7 (related to Figures 5 and 6). Dynamics of CHIN-1::GFP in a wild type embryo. Movie runs from maintenance onset to cleavage. Time compression = 60:1.

Supplementary Experimental Procedures

Strains

Strain Name	Genotype	Source
WH532	*ddIs?[Ppie-1::gfp::par-6; unc-119(+)]; chin-1(tm1909)/sC1 [dpy-1(s2170) let(gk597)]III*	Kumfer et al, 2010
KK1216	*it298[par-3::gfp]*	Kemphues, unpub.
EM270	*itIs167[Ppie-1::gfp::par-6; unc-119(+)]; par-2(lw32) unc-45(e286ts)/sC1[dpy-1(s2171)]III*	this study
EM217	*itIs167[Ppie-1::gfp::par-6; unc-119(+)]; par-2(lw32) unc-45(e286ts)/sC1[dpy-1s(2171)]III; lgl-1(tm2616)X*	this study
EM265	*itIs179[Ppar-3::par-3::gfp; unc-119(+)]; ddIs?[Ppie-1::mCherry::par-6; unc-119(+)]; chin-1(tm1909)/sC1 [dpy-1(s2170) let(gk597)]III*	this study
EM241	*itIs179[Ppar-3::par-3::gfp; unc-119(+)]; mrck-1(ok586)V/nT1 [qIs51] (IV;V)*	this study
EM266	*itIs179[Ppar-3::par-3::gfp; unc-119(+)]; par-2(lw32) unc-45(e286ts)/sC1[dpy-1(s2171)]III; lgl-1(tm2616)X*	this study
EM40	*itIs179[Ppar-3::par-3::gfp; unc-119(+)]; unc-119(ed3) III*	Li et at, 2010
WH363	*ojIs40[Ppie::gfp::wsp-1(G-Protein-Binding-Domain); unc-119(+)]; unc-119(ed3)III*	Kumfer et al, 2010
EM279	*ojIs69[Ppie-1::gfp::chin-1; unc-119(+)]; mrck-1(ok586)V/nT1 [qIs51] (IV;V)*	this study
EM221	*ojIs69[Ppie-1::gfp::chin-1; unc-119(+)]; par-2(lw32) unc-45(e286ts)/sC1[dpy-1(s2171)]III*	this study
EM212	*ojIs69[Ppie-1::gfp::chin-1; unc-119(+)]; par-2(lw32) unc-45(e286ts)/sC1[dpy-1(s2171)]III; lgl-1(tm2616)X*	this study
EM216	*ojIs69[Ppie-1::gfp::chin-1; unc-119(+)]; par-6(zu222) unc-10(m1)/hln1[unc-54(h1040)]I*	this study
WH497	*ojIs69[Ppie-1::gfp::chin-1; unc-119(+)]; unc-119(ed3)III*	Kumfer et al, 2010
MG589	*xsSi3[cb-unc-119(+); gfp::utrophin]*	Tse et al, 2012
EM290	*zuIs45[Pnmy-2::nmy-2::gfp; unc-119(+)]; par-2(lw32) unc-45(e286ts)/sC1[dpy-1s2171)]III*	this study
KK1140	*zuIs45[Pnmy-2::nmy-2::gfp; unc-119(+)]; par-2(lw32) unc-45(e286ts)/sC1[dpy-1s2171)]III; lgl-1(tm2616)X*	Beatty et al, 2013

RNA interference

L4 larvae were transferred to feeding plates and then cultured for 36-48 hours (16-24 hours for *gfp(RNAi)*) at 20˚C before imaging. For experiments involving *par-2(lw32)*, *chin-1(tm1909)* or *mrck-1(ok586)* mutants, we used heterozygotes cultured on the same feeding plates as controls. For experiments involving *mrck-1(RNAi)*, we used identically treated worms expressing an NMY-2::GFP transgene to verify strong loss of cortical NMY-2. For other RNAi experiments, we verified strong loss of function by observing 100% embryonic lethality and either symmetrical first cleavage (*par-2*, *par-3*, *par-6*, *pkc-3*, and *cdc-42)* or hyper-contraction of the anterior cortex during pseudocleavage and equally timed second cleavages (*par-1)*.

Image acquisition

For the experiments reported in Figures 2, 3, 6, S1, S2, S4 and S6B, we used a Nikon Ti-E inverted microscope equipped with solid state 50mW 481 and 561 Sapphire lasers (Coherent), a Yokogawa CSU-X1 spinning disk scan head, and a Ti-ND6-PFS Perfect Focus unit. We collected equatorial images (Figures 2C,F,G; 3; and S2A,B,D) using a 1.2NA 60x water immersion objective onto a Rolera em-c^2 EM-CCD camera with 30% laser power and 600 msec exposures. We collected surface images (Figures 2A,D,E; 5; 6 (excluding 6A); S1; S2C; S3E; and S4) using a CFI Apo 1.45 NA oil immersion TIRF objective onto an Andor iXon3 897 EMCCD camera using 30% laser power and exposure times from 200-500 msec; we used identical exposure times within each experiment for comparison across genotypes/RNAi conditions.

For the near-TIRF imaging experiments reported in Figures 4, 6A,D, S3, and S5, we used an Olympus IX71 inverted microscope equipped with an Olympus OMAC two-color TIRF illumination system, a CRISP autofocus module (Applied Scientific Instrumentation), and a 1.45 NA oil immersion TIRF objective. Laser illumination at 488 nm from a 50-mW solid-state Sapphire laser (Coherent) was delivered by fiber optics to the TIRF illuminator. Images were magnified by 1.6x and collected on an Andor iXon3 897 EMCCD camera, yielding a pixel size of 100 nm. Image acquisition was controlled by Andor IQ software. For all experiments, we set the laser illumination angle to a standard value that was chosen empirically to approximately maximize signal-to-noise ratio while maintaining approximately even illumination across the field of view. For MSD analysis and single molecule imaging, we collected data in stream acquisition mode using 20% (MSD analysis) or 100% (single molecule imaging) laser power and 50 msec exposures. For all other experiments, we collected images at 1 sec intervals using 40% laser power and 50 msec exposures.

Measuring cortical intensities of GFP::PAR-6 or GFP::wspGBD

We measured cortical intensities of GFP::PAR-6 or GFP::wspGBD from equatorial confocal sections using custom functions written in Matlab (*www.mathworks.com*). After smoothing each image with a 4x4 mean filter, we determined a threshold intensity value such that nearly all pixels within the embryo's interior were above threshold. We used this threshold to create a binary mask and then determined the smallest ellipse containing the mask and aligned with its long axis. We parameterized the boundary of this ellipse in terms of arc length $0 \leq s < 1$. For each of 200 discrete values of $s = s_i$, we assessed pixel intensities in the smoothed image

along rays perpendicular to the boundary, using $I = I_{smo} - I_{bgd}$, where I_{smo} is the smoothed intensity and I_{bgd} is the background intensity measured well outside the mask. Moving along each ray from the edge of the image towards the cell interior, we identified the first position at which I exceeded a threshold value defined as $I_{th} = 0.9 * \left(I_{\text{int}} - I_{bgd} \right)$, where I_{int} is the average intensity measured in a region of the posterior cytoplasm excluding the nucleus. We then measured boundary intensity in the original image at arc length s_i as the mean intensity measured for 300nm along the ray just beyond this threshold position, divided by the mean intensity measured over an additional distance of 2μm along the same ray within the cell interior. To control for variability of transgene expression in different genetic backgrounds, we normalized the intensity data for each embryo by the mean intensity within a region of posterior cytoplasm before calculating means and standard errors over multiple embryos.

Kymographs

We produced the kymographs shown in Figures 2A,D,E; S1B; S2C; and S6A,B using ImageJ (*imagej.nih.gov/ij/)* by the following method: from sequences of individual images, for each image, we selected a rectangular region of dimensions LxH aligned with the major axis of the embryo. We then used ImageJ's reslice and Z Project functions to obtain a single row of L pixels, each representing the maximum intensity projection of the rectangular region parallel to the long axis. We constructed the kymograph image by stacking these rows vertically and then scaled the resulting image vertically to its final size.

Measuring cortical flow velocities

We measured cortical flow velocities vs anterior/posterior (AP) position in embryos expressing NMY-2::GFP using Particle Image Velocimetry as follows: We collected movie frames using near-TIRF microscopy at 2-second intervals. Then we used a freely available PIV toolbox called mpiv (*www.oceanwave.jp/softwares/**mpiv***) to estimate local velocities of the cortical flow field. We used the Minimum Quadratic Differences algorithm with iterative refinement to a window size of 32x32 pixels, and 50% overlap between adjacent windows, to estimate frame-to-frame displacements with 1.6μm resolution. We averaged all displacements measured at a given AP position. Then we averaged these measurements over 30-40 frames (60-80 seconds) during the posterior and anterior contraction phases to obtain estimates of average flow vs AP position during each of these phases for a given embryo.

Single particle detection and localization.

To identify and localize single particles (both single molecules and clusters containing CHIN-1::GFP or PAR-3::GFP), we used a Matlab implementation (http://people.umass.edu/kilfoil/downloads.html) of the Crocker and Grier (Crocker, 1996) method. Briefly, in each image, the method uses a band pass filter to highlight roughly circular regions below a characteristic size (the feature size), in which the pixel intensity exceeds the background. The regions in which the maximum intensity exceeds a user-defined threshold are identified, and their centroids are

determined to sub-pixel resolution as the center of mass of pixel intensity within a pixelated circular mask centered on the original maximum.

For each particle type, we chose a feature size just large enough to ensure detection of the largest observable particles. We initially chose a detection threshold using two different methods: (1) we plotted the number of particles vs detection threshold and determined an inflection point at which the number of detected particles began to increase sharply due to increasing numbers of false positive detections, and (2) we determined a threshold subjectively as the minimum value for which all of the particles visible by eye in a given image were detected. The values chosen by these two methods were very nearly equal, and the differences between the values produced negligible effects on the quantities we report. Therefore, we used the subjective method to set the detection threshold for all of the analyses we report. In the case of PAR-3, the smallest particles are almost certainly monomers based on a direct comparison of these particle intensities to those measured under the same conditions in embryos expressing single molecule levels of PAR-3 (Fig. S3A). In the case of CHIN-1, single molecules are undetectable in zygotes expressing the transgene at normal levels, due to the higher level of rapidly diffusing non-clustered CHIN-1::GFP at the membrane.

Single particle tracking

To analyze singe molecule dynamics, CHIN-1 and PAR-3 cluster mobilities, and CHIN-1 cluster growth kinetics, we performed single particle tracking as follows. We used the Crocker-Grier algorithm as described above to identify and localize particles within individual frames. Then we used μTrack software (Jaqaman et al., 2008) to link these into particle trajectories.

μTrack performs tracking in two steps, first linking particles frame-to-frame into short segments and then linking these segments into longer trajectories. User-definable statistical models for particle motion are used to assign costs (probabilities) for the different possible linkage assignments, including particle appearance, disappearance, displacement, fusion and fission. The algorithm then seeks to globally minimize these costs. For our analysis, we used one of the built-in statistical motion models provided with μTrack that represents a mixture of Brownian and direct motion; we allowed the possibility of "gaps" in trajectories of up to 6 frames due to transient failure to detect particles in individual frames.

For the analysis PAR-3 and CHIN-1 cluster mobilities and growth rates, we allowed for the detection of particle fusion and fission events. For all subsequent analyses, and for the trajectories plotted in Figure 6C&D, we considered only the portions of each trajectory that lay between fusion and fission events, and we treated each of these as a separate trajectory.

Measuring background-subtracted fluorescence intensity for individual particles

To measure a background-subtracted intensity associated with each detected particle in each frame, we first measured the total pixel intensity (I_{tot}) in the original image under a circular mask, centered on the particle centroid, with radius equal to the feature size. Then we determined the average pixel intensity (I_{bg}) within an annular region, two pixels in width, surrounding this mask. Then we computed the background-subtracted intensity as:

$$I = I_{tot} - A_{mask} * I_{bg} ,$$

where A_{mask} is the area of the circular mask.

To measure particle density, mean particle intensity and total fluorescence intensity per unit area as a function of axial position, we used ImageJ to trace the boundary of the region in which particles were in focus at the surface of the embryo. In Matlab, we fit an ellipse to this boundary and determined its major, or anterior-posterior (AP) axis. We projected the boundary onto the AP axis to obtain maximum and minimum boundary positions b_{min} and b_{max}. We then projected the position of each particle onto the same AP axis and then used that position relative to b_{min} and b_{max} to assign the particle to one of 20 bins of equal width along the AP axis. Within each bin, we then determined the total number of particles and their mean (background-subtracted) intensity. We measured the particle density as the number of particles divided by the bin's area. Then we defined and measured the mean fluorescence intensity as the particle density times the mean particle intensity.

Analysis of CHIN-1 cluster trajectories

To analyze intensity vs time for individual CHIN-1::GFP cluster trajectories, we measured background-subtracted cluster intensities for each time point within the trajectory as described above. We smoothed the data using a 5 frame moving average. These smoothed intensity data are plotted for individual trajectories in Figure 6E. We measured the instantaneous

cluster growth rate as the frame-to-frame difference in these smoothed intensities and used these values to assign colors to each trajectory subsegment in Figure 6D. To plot mean growth rate vs axial position (Figure 6F), we used the method described above to assign instantaneous growth rates for all particle positions within all trajectories into 20 bins of equal width aligned with the long axis of the embryo.

MSD analysis

To perform MSD analysis of PAR-3::GFP and GFP::CHIN-1 clusters, we imaged embryos at 20 frames/sec in near-TIRF mode using laser power (20% of the 50mW laser) that yielded an adequate signal-to-noise ratio while reducing photobleaching rates to acceptable levels. We detected particles within each frame using the Crocker-Grier algorithm and then used μTrack to determine particle trajectories as described above. As above, we assumed a mixture of Brownian and directed motion, allowed for "gaps" of up to 6 frames, and considered the portions of each trajectory that lay between merge and split events as separate trajectories.

For PAR-3::GFP, we analyzed movies containing 2000-3000 frames (100-150 sec) taken during the early-mid maintenance phase, and we limited our analysis to the anterior domain containing high levels of PAR-3 and excluding the posterior boundary of this domain where cortical flows are pronounced. For CHIN-1::GFP, we used an *mrck-1(ok586)* mutant background to factor out myosin contractility. We analyzed movies containing 4000 frames (200 sec) from early maintenance phase onward, and we restricted our analysis to the posterior domain in which CHIN-1 clusters are enriched.

For each movie, we considered all particle trajectories with length greater than five frames. For each lag time τ (in frames), we partitioned every trajectory into contiguous, non-overlapping segments of length τ; for each segment, we computed the mean-square-displacement as $x^2 = \left(x_f - x_i\right)^2$, where x_i and x_f are the initial and final centroid positions within each segment. We then computed the mean-square-displacement for each τ as:

$$\left\langle x^2 \right\rangle = \frac{\sum_{all\ segments\ i} x_i^2}{N}$$

where N is the total number of segments of length τ. We plotted data only for those lag times for which we had > 100 independent measurements.

Analysis of PAR-6::GFP single molecule appearance events.

We performed single molecule imaging as described previously (Robin et al., 2014). Briefly, we used RNAi directed against the GFP sequence to reduce expression of the GFP::PAR-6 transgene to near single molecule levels. Then we imaged embryos at 20 frames per second under continuous laser illumination using 100% of the 50mW laser. As shown previously (Robin et al., 2014), this results in rapid (within 2-3 seconds from the onset of illumination) relaxation to a quasi-steady state in which approximately constant densities of GFP::PAR-6 molecules are maintained for many minutes because molecules that photobleach (or dissociate)

are replaced by new molecules that bind from the cytoplasmic pool. Under these imaging conditions, the signal to noise ratio is greater than 5, allowing for highly accurate single molecule detection (Robin et al, 2014). We empirically adjusted the GFP::PAR-6 levels so that at this quasi-steady state, the mean frame-to-frame displacement of single molecules was less than 10% of the average distance between molecules, allowing for highly accurate reconstruction of single molecule trajectories using μTrack (Jaqaman et al, 2008).

For each embryo, we recorded 2000 frames, from the beginning of maintenance phase, at 20 frames per seconds (100 s total) under the quasi-steady state conditions described above. We used the Crocker-Grier algorithm to detect single molecules and μTrack to construct single molecule trajectories, as described above. Ignoring trajectories of length less than 3 frames, we scored the beginning of each trajectory as an appearance event. We mapped all appearance events recorded during the 100s interval to 20 bins equally spaced along the AP axis, as described above; then we divided by the area of each bin and the elapsed time to determine a mean appearance rate per unit area and time.

Supplemental Modeling Procedures

A mathematical model of the CDC-42/CHIN-1 subcircuit.

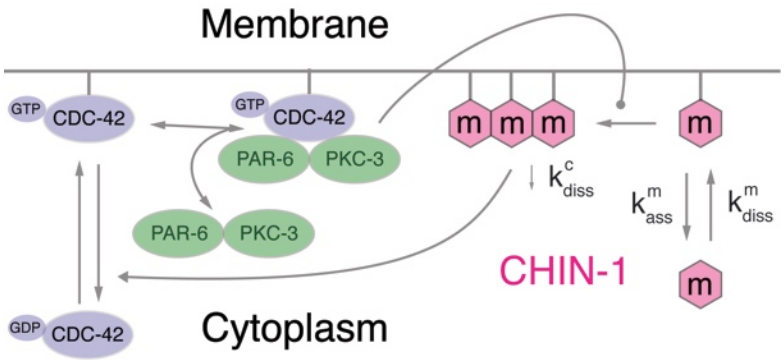

Figure A1

Here we construct and analyze a minimal model of the CDC-42/CHIN-1 circuit based on the schematic diagram shown above and in Figure 8a. We focus on a scenario in which PAR-1 is absent and posterior levels of PAR-3 are not limiting for recruitment of PAR-6/PKC-3. We assume: (a) that CDC-42 cycles between inactive (cytoplasmic) and active (membrane-bound) states; (b) that PAR-6 and PKC-3 form a stable heterodimer, which resides in the cytoplasm and binds reversibly to active CDC-42 to form a membrane-bound CDC-42/PAR-6/PKC-3 trimer; (c) that CHIN-1 monomers bind reversibly to the membrane where they self-assemble into larger clusters and (c) that membrane-bound CHIN-1 promotes local inactivation of CDC-42 at a rate proportional to the product of the local concentrations of CHIN-1 and CDC-42.

Because the molecular basis for CHIN-1 clustering is unknown, we use a simple phenomenological description that is consistent with our data and that captures our key hypothesis that CHIN-1 clusters form through a cooperative assembly process. First, we assume

that there is a critical concentration of CHIN-1 monomers above which net cluster assembly occurs. Letting λ be this critical concentration, h be the total density of CHIN-1 subunits at the membrane and h_m and h_c be the densities of CHIN-1 subunits in monomer and cluster form respectively, we write:

(1)
$$h_m = \left\{ \begin{array}{ll} h: & h < \lambda \\ \lambda: & h \geq \lambda \end{array} \right\}$$
$$h_c = \left\{ \begin{array}{ll} 0: & h < \lambda \\ h - \lambda: & h \geq \lambda \end{array} \right\}$$

Second, we assume that CHIN-1 monomers bind weakly to the membrane, and that association into clusters leads to an increase in binding avidity. For simplicity, we assume that this increase in avidity can be captured through two dissociation rates: a fast monomer dissociation rate k^m_{diss}, and a slower mean cluster dissociation rate k^c_{diss}. With these assumptions, we write the mean dissociation rate for all CHIN-1 (monomers and clusters) as:

(2)
$$\overline{k}^h_{diss} = \left\{ \begin{array}{ll} k^m_{diss}: & h < \lambda \\ \dfrac{k^m_{diss}\,\lambda + k^c_{diss} * (h - \lambda)}{h}: & h \geq \lambda \end{array} \right\}$$

As discussed in the main text, PAR-6/PKC-3 could inhibit clustering of CHIN-1 either by increasing the critical concentration for cluster assembly or by modulating the size of the monomer pool. We focus on the first scenario, but the second yields identical results and

conclusions (see below). Letting p represent the concentration of the CDC-42/PAR-6/PKC-3 trimer, and assuming that PAR-6/PKC-3 modulates the critical concentration via $\lambda = \lambda^0 + \eta p$, the mean dissociation rate for h can be expressed as a function of p:

(3) $$k_{diss}^{h}(p) = \left\{ \begin{array}{ll} k_{diss}^{m} : & p > \dfrac{h-\lambda^0}{\eta} \\ \dfrac{k_{diss}^{m} * \lambda + k_{diss}^{c} * (h-\lambda)}{h} : & p \le \dfrac{h-\lambda^0}{\eta} \end{array} \right\}$$

With these assumptions, letting *c* and *h* represent the surface densities of CDC-42 and CHIN-1, respectively, and neglecting depletion of cytoplasmic pools, we write:

(4) `

where $k_{ass}^{x}, k_{diss}^{x}$ are association and dissociation rate constants, and β_c represents the strength of CDC-42 inactivation by CHIN-1.

We define new dimensionless variables $\bar{c} = \dfrac{c}{K_c}$, $\bar{p} = \dfrac{p}{K_p}$, and $\bar{h} = \dfrac{h}{K_h}$, where $K_c = \dfrac{k_{ass}^{c}}{k_{diss}^{c}}$,

$K_p = \dfrac{k_{ass}^{p}}{k_{diss}^{p}}$ and $K_h = \dfrac{k_{ass}^{h}}{k_{diss}^{c}}$ are the maximum levels reachable respectively by *c*, *p* and *h*.

Rearranging terms and dropping the caps over $\bar{c}$, $\bar{p}$, and $\bar{h}$ yields:

(5)
$$\frac{dc}{dt} = k^c_{diss}\left(1-\left(1+\hat{\beta}_c h\right)c\right) - k^p_{diss}(c-p)$$
$$\frac{dp}{dt} = k^p_{diss}(c-p)$$
$$\frac{dh}{dt} = k^c_{diss}\left(1-\left\{\begin{array}{ll} \alpha h: & p > \dfrac{h-\hat{\lambda}^0}{\hat{\eta}} \\ \alpha\hat{\lambda}+h-\hat{\lambda}: & p \le \dfrac{h-\hat{\lambda}^0}{\hat{\eta}} \end{array}\right\}\right)$$

where $\hat{\beta}_c = \frac{\beta_c K_h}{k^c_{diss}}$, $\hat{\lambda} = \hat{\lambda}^0 + \hat{\eta}p$, $\hat{\lambda}^0 = \frac{\lambda^0}{K_h}$, $\hat{\eta} = \frac{\eta K_c K_p}{K_h}$ and $\alpha = \frac{k^m_{diss}}{k^c_{diss}}$ are dimensionless ratios

of the original parameters.

Analyzing the steady state behavior of the CDC-42/CHIN-1 circuit

We analyze the steady state behavior of this system by setting $\frac{dc}{dt} = \frac{dp}{dt} = \frac{dh}{dt} = 0$ and

solving algebraically for the c, p, and h nullclines:

$$c = \frac{1}{1+\hat{\beta}_c h}$$
$$p = c$$

(6)
$$h = \left\{\begin{array}{ll} \dfrac{1}{\alpha}: & p > \dfrac{h-\hat{\lambda}^0}{\hat{\eta}} \\ 1-(\alpha-1)\left(\hat{\lambda}^0+\bar{\eta}p\right): & p \le \dfrac{h-\hat{\lambda}^0}{\hat{\eta}} \end{array}\right\}$$

Using $p = c$ to eliminate c, we obtain a projection of the p and h nullclines onto the p/h plane:

$$p = \frac{1}{1+\hat{\beta}_c h}$$

(7)

$$h == \left\{ \begin{array}{ll} \frac{1}{\alpha}: & p > \frac{h-\hat{\lambda}^0}{\hat{\eta}} \\ 1-(\alpha-1)\left(\hat{\lambda}^0+\bar{\eta}p\right): & p \le \frac{h-\hat{\lambda}^0}{\hat{\eta}} \end{array} \right\}$$

Equations (7) can be rewritten as:

$$p = \frac{1}{1+\hat{\beta}_c h}$$

(8)

$$h == \left\{ \begin{array}{ll} h_{\min}: & p > p_{th} \\ h_{\max} + \frac{(h_{\min}-h_{\max})}{p_{th}} p: & p \le p_{th} \end{array} \right\}$$

where $p_{th} = \frac{1-\alpha\hat{\lambda}^0}{\alpha\hat{\eta}}$; $h_{\min} = \frac{1}{\alpha} = \frac{k_{diss}^c}{k_{diss}^m}$ and h_{max}=1-$(\alpha-1)\lambda^0$.

Plotting the nullclines (Figure A2), one can readily see that there exist values of p_{th}, $h_{\min}$, h_{max}, and $\hat{\beta}_c$ for which the nullclines cross three times, a minimal condition for the system to exhibit bistability.

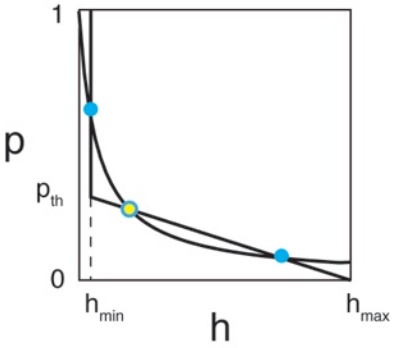

Figure A2

Using experimental observations to determine values for key model parameters.

To ask whether the CDC-42/CHIN-1 circuit is tuned in the zygote to yield bistable dynamics, we can estimate the values of these parameters from the measured distributions of CHIN-1, active CDC-42, and PAR-6. To facilitate this comparison, we note first that levels of GFP::PAR-6 and GFP::wspGBD at the posterior pole during mid-late maintenance are indistinguishable from cytoplasmic background and can thus be equated to the value of 0 for the scaled model variables *c* and *p*. Second, based on the complete lack of CHIN-1 clusters at the anterior and any detectable enrichment of unclustered CHIN-1 relative to cytoplasmic background, we assume that $h_{\min} \approx 0$, and we equate h_{max} to the maximum plateau level of CHIN-1 measured at the posterior pole in late maintenance phase. Finally, we assume that the values measured for GFP::PAR-6 and GFP::wspGBD at the anterior pole are maximal (i.e. the effects of low levels of CHIN-1 are minimal) and that we can therefore equate these maximum levels to a value of 1 for the scaled model variables c and p.

To estimate the value of the threshold p_{th}, we compared the mean position at which CHIN-1 clusters switch from growth to decay (~60% egg length; Figure 7I) to the mean steady state profile of GFP::PAR-6 (Figure 2E; Figure A3). Based on this comparison, we estimate $p_{th} = 0.17$.

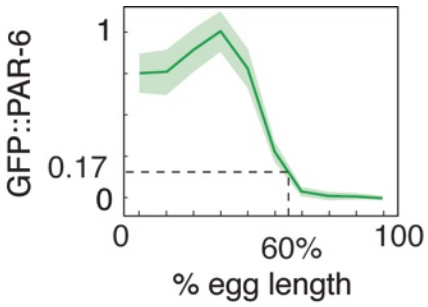

Figure A3

To estimate a value for $\hat{\beta}_c$, we first recall from equations (6) that $p = c$ at steady state and thus the p and c nullclines are identical:

(9) $$p = c = \frac{1}{1 + \hat{\beta}_c h}$$

Equation 9 represents the steady-state level of active CDC-42 for a given concentration of CHIN-1. We can estimate this by comparing mean values of GFP::wspGBD (active CDC-42) and CHIN-1::GFP that were measured at the posterior pole over time and aligned with respect to the onset of maintenance phase (Figure 8D; Figure A4, left). That is, given the two time series [CHIN-1](t_i) and [CDC-42](t_i), we can plot the pairs of values ([CHIN-1](t_i), [CDC-42](t_i)) (Figure A4, right).

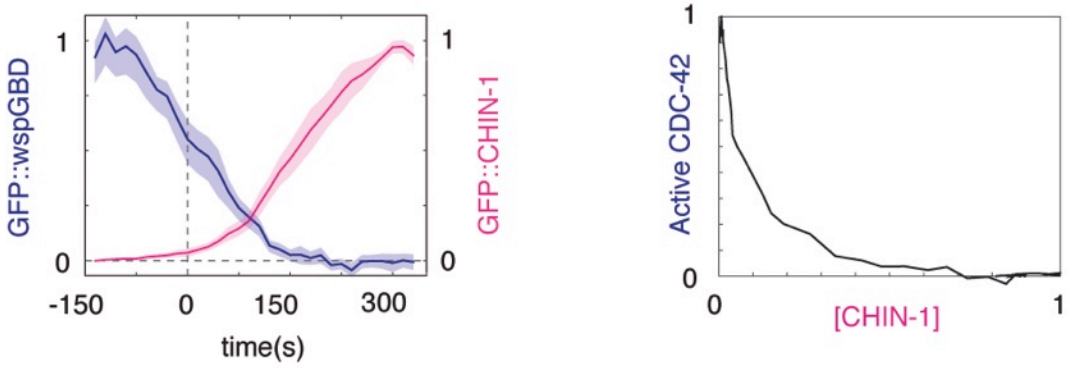

Figure A4

As shown below (Figure A5, left), a non linear least squares fit of $c = \frac{1}{1 + \hat{\beta}_c h}$ to this empirical relationship fails to capture the very sharp fall off of active CDC-42 with increasing CHIN-1.

We obtained a better fit using $c = \frac{1}{1+\beta_1 h+\beta_2 h^2}$ (Figure A5, right). This corresponds to the

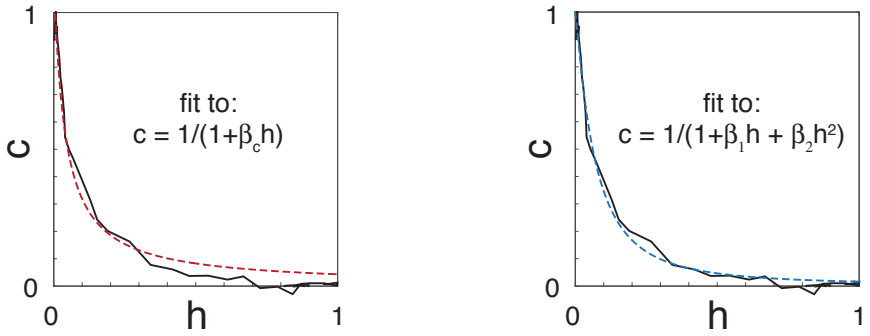

Figure A5

assumption (see below) that the dissociation rate for c is given by $k^c_{diss}\left(1+\beta_1 h+\beta_2 h^2\right)$.

Figure A6 shows plots of h and p nullclines using our estimates for p_{th} and either the empirical relationship between CHIN-1 and active CDC-42 (Figure A6, left) or using the non-linear least squares estimates for β_1 and β_2 assuming that $c = \frac{1}{1+\beta_1 h+\beta_2 h^2}$ at steady state (Figure A6, right).

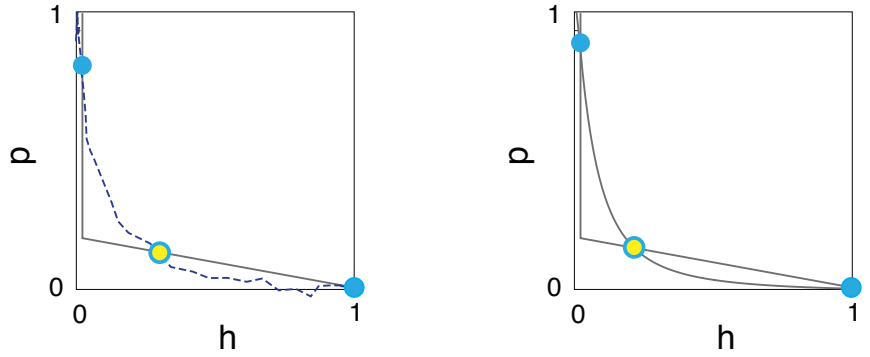

Figure A6

For either case, the nullclines cross three times, and one can verify analytically (not shown) or by simulation (Figure 7C) that the crossings shown in solid blue are stable steady states.

Based on this analysis, we conclude that the CDC-42/CHIN-1 system is in fact likely to be tuned into a regime where it exhibits bistable dynamics. We note that this prediction is insensitive to the exact shape of the h nullcline. Thus, while considering further details of 2D cluster assembly such as size-dependent growth kinetics might change the exact form of this steady state dependence, it is unlikely to change the basic conclusions of the analysis.

Adding diffusion and transport (of CHIN-1 clusters) to model spatiotemporal pattern formation.

To explore spatiotemporal dynamics produced by the CHIN-1/CDC-42 circuit, we introduced diffusion and transport terms into the scaled equations (5)

$$
\begin{aligned}
&\frac{dc}{dt} = -D_c \frac{\partial^2 c}{\partial x^2} + k_{diss}^c \left(1 - \left(1 + \beta_1 h + \beta_2 h^2\right) c\right) - \hat{k}_{diss}^p \left(c - p\right) \\
&\frac{dp}{dt} = -D_p \frac{\partial^2 p}{\partial x^2} + k_{diss}^p \left(c - p\right) \\
&\frac{dh}{dt} = -\frac{\partial (hv(x))}{\partial x} - D_h \frac{\partial^2 h}{\partial x^2} + k_{diss}^c \left(1 - \left\{ \begin{array}{ll} \alpha h: & h < \hat{\lambda} \\ \alpha\hat{\lambda} + h - \hat{\lambda}: & h \geq \hat{\lambda} \end{array} \right\}\right) \\
&\hat{\lambda} = \hat{\lambda}^0 + \hat{\eta} p
\end{aligned}
\qquad (10)
$$

The first term on the right hand side of the equation for h represents transport of h clusters with a cortical flow given by v(x) (Figure A7). Note that we have introduced polynomial

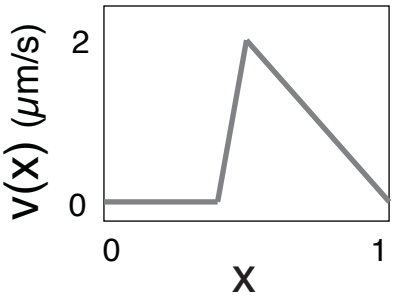

Figure A7

dependence of c dissociation on h following the above discussion, with new dimensionless parameters β_1 and β_2. We solved these equations numerically on a one-dimensional domain 0 < x < L, using zero-flux boundary conditions at x = 0 and x = L. This approach neglects the curvature-dependence of local diffusion and transport on the 2D embryo surface. Although it is possible to capture these effects by modeling the embryo as a prolate spheroid, the differences in the predicted dynamics are expected to be small (Goehring et al, 2011), especially near the equator where the curvature vanishes. Because we are primarily interested in the stability of the AP boundary that lies very near the equator, we chose to ignore curvature altogether.

Choosing parameter values

Following the above analysis, we set p_{th} to 0.17, h_{min} to a very low value (0.01), and h_{max} to its theoretical maximum of 1 in equations (9); then we determined values for $\alpha, \hat{\lambda}^0$ and $\hat{\eta}$ from $p_{th} = \frac{1-\alpha\hat{\lambda}^0}{\alpha\hat{\eta}}$, $h_{\min} = \frac{1}{\alpha}$ and h_{max}=1-$(\alpha-1)\lambda^0$. Based on the fits shown in Figure A4, right graph, we set $\alpha = 13.3$ and $\beta = 61.8$. Assuming that most of the PAR-6/PKC-3 in the posterior is associated with CDC-42 implies that the dissociation rate for CDC-42 must be slower than the measured dissociation rate for GFP::PAR-6 (Goehring et al, 2011a, Robin et al, 2014). For simplicity, we assume that these two rates are identical and equal to 0.01/s, which is close to the values measured by both Robin et al (2014) and Goehring et al (2011). Likewise, we assumed identical diffusivities for c and p, and set these to $D_c = D_p = 0.017\ \mu m^2/s$, based on

values measured by Robin et al (2014), which agree well with values reported by Goehring et al (2011). Given the very slow, subdiffusive mobility measured for CHIN-1 clusters (Figure S6A), and given that even the smallest detectable clusters couple strongly to cortical flow, we set $D_h = 0$, and we assumed 100% of CHIN-1 is transported by cortical flow at local velocity v(x) (see Figure A7). Finally, we set the dissociation rate for CHIN-1 monomers $k^m_{diss} = 0.5 / s$, and used $k^c_{diss} = \frac{k^m_{diss}}{\alpha}$ to determine the value of k^c_{diss}

Table A1. Simulation parameters.

Parameter	meaning	value	source/justification
k^p_{diss}	dissociation rate constant for p	0.01	Goehring et al (2011a) Robin et al (2014)
k^c_{diss}	basal inactivation rate constant for CDC-42	0.01	assumed to be same as k^p_{diss}
β_1	strength of CDC-42 inactivation by CHIN-1	13.3	Estimated by fitting p nullcline to data for [CHIN-1] vs [active CDC-42] (Figures A4, A5)
β_2	strength of CDC-42 inactivation by CHIN-1	61.8	Estimated by fitting p nullcline to data for [CHIN-1] vs [active CDC-42] (Figures A4, A5)
p_{th}	Threshold level of p at which h clusters switch from growth to decay	0.17	Estimated from comparison of steady state distribution of GFP::PAR-6 to CHIN-1 cluster growth rate vs AP position (Figure A2)
$h_{\max}$	maximum achievable level of h	1	scaled to 1

Parameter	meaning	value	source/justification
$h_{\min}$	minimum level of h achieved when p < p_{th}	0.01	Based on negligibly low levels of CHIN-1 at anterior pole.
D_p	Diffusivity of PAR-6/ PKC-3	0.17	Robin et al (2014)
D_c	Diffusivity of CDC-42	0.17	Assumed to be the same as D_p
D_h	Diffusivity of CHIN-1 clusters	0	measured in this paper Figure S6A
α	ratio of monomer to mean cluster dissociation rate for CHIN-1	100	calculated from $h_{\min} = \frac{1}{\alpha}$
λ^0	Critical concentration for CHIN-1 cluster growth in the absence of PAR-6/ PKC-3	0	calculated from $h_{\max} = 1 - (\alpha - 1)\lambda^0$
η	steepness of dependence of critical concentration on PAR-6/PKC-3	0.059	calculated from $p_{th} = \frac{1 - \alpha\hat{\lambda}^0}{\alpha\hat{\eta}}$

What if PAR-6/PKC-3 promote CHIN-1 monomer dissociation instead of tuning critical concentration for cluster growth?

We now consider the scenario in which, instead of tuning the critical concentration for cluster assembly, PAR-6/PKC-3 promotes CHIN-1 monomer dissociation at a rate that is

proportional to the product their concentrations. In this scenario, the equations for c and p remain unchanged, and the equation for h becomes:

$$\frac{dh}{dt} = k_{ass}^{h} - \left\{ \begin{array}{ll} k_{diss}^{mon}\left(1+\beta_h p\right)h: & h<\lambda \\ k_{diss}^{mon}\left(1+\beta_h p\right)\lambda + k_{diss}^{pol}\left(h-\lambda\right): & h\geq\lambda \end{array} \right\} \tag{11}$$

where β_h is the strength with which p promotes CHIN-1 dissociation. We non-dimensionalize as above, using $K_c = \frac{k_{ass}^{c}}{k_{diss}^{c}}; \quad K_p = \frac{k_{ass}^{p}}{k_{diss}^{p}}; \quad K_h = \frac{k_{ass}^{h}}{k_{diss}^{poly}}; \quad \alpha = \frac{k_{diss}^{mon}}{k_{diss}^{poly}}$. K_c, defining new dimensionless variables $\bar{c} = \frac{c}{K_c}$, $\bar{p} = \frac{p}{K_p K_c}$ and $\bar{h} = \frac{h}{K_h}$, then rearranging terms and dropping the bars to obtain:

$$\frac{dh}{dt} = k_{diss}^{poly}\left(1 - \left\{ \begin{array}{ll} \alpha\left(1+\hat{\beta}_h p\right)h: & h<\hat{\lambda} \\ \alpha\left(1+\hat{\beta}_h p\right)\hat{\lambda} + (h-\hat{\lambda}): & h\geq\hat{\lambda} \end{array} \right\}\right) \tag{12}$$

where $\hat{\beta}_h = \beta_h K_p$ and $\hat{\lambda} = \frac{\lambda}{K_h}$ are dimensionless ratios of the original parameters.

setting $\frac{dh}{dt} = 0$ and solving algebraically yields:

(13) $$h = \left\{ \begin{array}{ll} \dfrac{1}{\alpha\left(1+\hat{\beta}_h p\right)}: & h < \hat{\lambda} \\ 1-\left(\alpha\left(1+\hat{\beta}_h p\right)-1\right)\hat{\lambda}: & h > \hat{\lambda} \end{array} \right\}$$

Again, we can simplify by rewriting:

(14) $$h == \left\{ \begin{array}{ll} \dfrac{1}{\alpha\left(1+\hat{\beta}_h p\right)}: & p > p_{th} \\ h_{\max} + \dfrac{\left(\hat{\lambda} - h_{\max}\right)}{p_{th}} p: & p \le p_{th} \end{array} \right\}$$

where $p_{th} = \dfrac{1-\hat{\lambda}\alpha}{\hat{\beta}_h \hat{\lambda}\alpha}$ and $h_{\max} = 1-(\alpha-1)\hat{\lambda}$.

Comparing equations (8) and (14), we see that there are two main differences: the threshold p_{th} scales inversely with by $\hat{\beta}_h$ instead of η, and instead of remaining constant for $p > p_{th}$, the value of h falls towards 0. Neither of these differences affect the basic conclusion that the system may be tuned into a regime in which it can exhibit bistable dynamics. For the simulations described below, we assumed that PAR-6/PKC-3 act by tuning the critical concentration for cluster growth.

Modeling the PAR-1/PAR-3 subcircuit.

Here we show that the PAR-1/PAR-3 subcircuit could also yield bistable dynamics if PAR-3 oligomers undergo cooperative assembly that is inhibited by PAR-1. We make the following assumptions:

(1) PAR-1 binds reversibly to the plasma membrane.

(2) PAR-3 monomers bind reversibly to the plasma membrane; membrane-bound PAR-3 oligomers assemble above a critical monomer concentration, and the avidity of PAR-3 increases with oligomer size.

(3) CDC-42 is uniformly distributed as in *chin-1* mutants, and PAR-3 acts locally to promote association of PAR-6/PKC-3 with CDC-42 to form an active membrane-bound complex.

(4) PAR-1 acts by increasing the critical concentration for PAR-3 oligomerization.

(5) The PAR-6/PKC-3 dimer promotes local dissociation of PAR-1 at a rate that is proportional to the product of the concentrations of PAR-6/PKC-3 and PAR-1.

Letting p_1 = [PAR-1], p_k = [PAR-6/PKC-3] and p_3 = [PAR-3], and defining

$$K_{p1} = \frac{k_{ass}^{p1}}{k_{diss}^{p1}}; \quad K_{pk} = \frac{k_{ass}^{pk}}{k_{diss}^{pk}}; \quad K_{p3} = \frac{k_{ass}^{p3}}{k_{diss}^{poly}}; \quad \alpha = \frac{k_{diss}^{mon}}{k_{diss}^{poly}},$$ we write:

(15)

$$\frac{dp_1}{dt} = k_{diss}^{p_1}\left(K_{p1} - \left(1+\beta_{p1}p_k\right)p_1\right)$$
$$\frac{dp_k}{dt} = k_{diss}^{pk}\left(K_{pk}p_3 - p_k\right)$$
$$\frac{dp_3}{dt} = k_{diss}^{poly}\left(K_{p_3} - \left\{\begin{array}{ll} \alpha p_3: & p_3 < \lambda \\ \alpha\lambda + p_3 - \lambda: & p_3 \geq \lambda \end{array}\right\}\right)$$
$$\lambda = \lambda^0 + \eta p_1$$

We non-dimensionalize as above, defining $\bar{p}_1 = \frac{p_1}{K_{p_1}}$, $\bar{p}_k = \frac{p_k}{K_{p_k}K_{p_3}}$ and $\bar{p}_3 = \frac{p_3}{K_{p_3}}$, then

rearranging terms and dropping bars to obtain:

(16)

$$\frac{dp_1}{dt} = k_{diss}^{p_1}\left(1 - \left(1+\hat{\beta}_{p1}p_k\right)p_1\right)$$
$$\frac{dp_k}{dt} = k_{diss}^{pk}\left(p_3 - p_k\right)$$
$$\frac{dp_3}{dt} = k_{diss}^{poly}\left(1 - \left\{\begin{array}{ll} \alpha_{diss}p_3: & p_3 < \hat{\lambda}_{p_3} \\ \alpha_{diss}\hat{\lambda}_{p_3} + p_3 - \hat{\lambda}_{p_3}: & p_3 \geq \hat{\lambda}_{p_3} \end{array}\right\}\right)$$
$$\hat{\lambda}_{p_3} = \hat{\lambda}_{p_3}^0 + \hat{\eta}_{p_3}p_1$$

where $\hat{\beta}_{p_1} = \beta_{p_1}K_{p_k}K_{p_3}$, $\hat{\lambda}^0 = \frac{\lambda^0}{K_{p_3}}$ and $\hat{\eta} = \frac{\eta K_{p_1}}{K_{p_3}}$ are dimensionless ratios of the original parameters.

setting $\frac{dp_1}{dt} = \frac{dp_k}{dt} = \frac{dp_3}{dt} = 0$ and solving algebraically for the p_1, p_k and p_3 nullclines:

$$p_1 = \frac{1}{1+\hat{\beta}_{p_1} p_k}$$

$$p_3 = p_k$$

(17)

$$p_3 = \left\{ \begin{array}{ll} \frac{1}{\alpha}: & p_1 > \frac{p_3 - \hat{\lambda}^0}{\hat{\eta}} \\ 1-(\alpha-1)\left(\hat{\lambda}^0 + \bar{\eta} p_1\right): & p_1 \le \frac{p_3 - \hat{\lambda}^0}{\hat{\eta}} \end{array} \right\}$$

Because $p_3 = p_k$ at steady state, the p and c nullclines are identical, and we can eliminate p_3 to obtain a projection of the p_1 and p_k nullclines onto the p_1/p_k plane:

$$p_1 = \frac{1}{1+\hat{\beta}_{p_1} p_k}$$

(18)

$$p_k = \left\{ \begin{array}{ll} \frac{1}{\alpha}: & p_1 > \frac{p_k - \hat{\lambda}^0}{\hat{\eta}} \\ 1-(\alpha-1)\left(\hat{\lambda}^0 + \bar{\eta} p_1\right): & p_1 \le \frac{p_k - \hat{\lambda}^0}{\hat{\eta}} \end{array} \right\}$$

At this point, we can see clearly that the forms of the equations for the p_1 and p_k nullclines are identical to those for p and h in equations (7), and therefore we conclude without any further analysis that this system can also yield bistable dynamics.

Supplemental References

Crocker, J. (1996). Methods of Digital Video Microscopy for Colloidal Studies. Journal of Colloid and Interface Science *179*, 298–310.

Goehring, N.W., Trong, P.K., Bois, J.S., Chowdhury, D., Nicola, E.M., Hyman, A.A., and Grill, S.W. (2011b). Polarization of PAR proteins by advective triggering of a pattern-forming system. Science *334*, 1137–1141.

Jaqaman, K., Loerke, D., Mettlen, M., Kuwata, H., Grinstein, S., Schmid, S.L., and Danuser, G. (2008). Robust single-particle tracking in live-cell time-lapse sequences. Nat Meth *5*, 695–702.

Tse, Y.C., Werner, M., Longhini, K.M., Labbé, J.-C., Goldstein, B., and Glotzer, M. (2012). RhoA activation during polarization and cytokinesis of the early Caenorhabditis elegans embryo is differentially dependent on NOP-1 and CYK-4. Mol Biol Cell *23*, 4020–4031.